Visualization and Reduction of Mutual Coupling Between Antennas Installed on a Platform

Johan Lundgren, Johan Malmström, Jari-Matti Hannula, and B. L. G. Jonsson

***Abstract*—Mutual coupling, or equivalently, the isolation between antennas, is a key parameter in antenna system design. In this work, the previously defined impedance density is generalized, and it is demonstrated how it can be used to obtain spatial information about the mutual coupling. The generalized impedance density is a real-valued scalar and it can be visualized as a three-dimensional density in space. It is shown that there is a strong connection between regions with a positive (negative) generalized impedance density and a decrease (increase) of the coupling when an absorber is placed in that region. This predictive ability is a useful feature, which is tested for three numerical cases. The results are robust to the shape of the platform, and it can be compared across frequencies. By placing absorbers based on the generalized impedance density, it is possible to reduce the required amount of absorbers needed to obtain a certain reduction in mutual coupling. The visualization results and predictions of absorber positions are compared with a Poynting vector based method. Placing absorbers based on the generalized impedance density had a larger impact on the mutual coupling, compared to the predictions with the Poynting vector based method in the investigated cases.**

***Index Terms*—Mutual coupling, isolation, visualization, reciprocity, reaction theorem.**

I. Introduction

LOW isolation between antennas can degrade the overall system performance, since the transmitted power of one antenna may leak into a receiving antenna of another system. This makes mutual coupling between antennas one of the key parameters for antenna system performance [1], in particular for antennas on vehicles where the distance between antennas is strongly constrained. Methods to reduce mutual coupling between antennas date back to early antenna constructions [2]. A few recent publications on the subject include [3], [4] that utilized parasitic elements and [5]–[7], where electromagnetic bandgap structures [8] have been used. In [7], the possibility of using ferrite absorbers is also studied.

For complex vehicle platforms such as airplanes and ships, the mutual coupling consists of several contributions such as line-of-sight, edge-diffraction, creeping waves, and reflection coupling [1], [9], which complicate the process of placing absorbers to mitigate the mutual coupling. A visualization method should describe all the above-mentioned mechanisms to be a useful tool for identifying regions with strong contributions to the mutual coupling. A path between a transmitting and receiving antenna that depicts the spatial contribution to the mutual coupling is referred to as a coupling path [10]–[13].

Several methods to visualize mutual coupling have been suggested in the literature, including ray-tracing and diffuse scattering [14], [15]. These methods are generally not applicable to antennas installed on platforms since the near-field contribution can substantially contribute to the coupling.

A Poynting vector based method was defined [12], [13] and applied [16], [17] to mitigate electromagnetic interference. In these works, the coupling paths are visualized by computing streamlines through the power flow between the receiving and transmitting antennas. The Poynting vector based method, in its current form, does not distinguish between the incident and accepted power. Also, as seen in [17], the streamlines follow different paths depending on which antenna is transmitting and receiving, even though the setup is reciprocal, see [18].

In our previous paper [10], a *normalized impedance density* was defined using the reaction theorem [19]–[21]. It was proposed that paths of strong positive normalized impedance density are indeed coupling paths. A method to test this idea with a small absorber was also proposed. However, no such validation results were presented at the time. In the present paper, we follow up and improve on this idea. We here provide both a theoretical motivation between coupling paths and the impedance density and illustrate a numerical validation of coupling paths. We show that the real-part of a suitably normalized impedance density is directly related to the mutual impedance and that it indeed can be interpreted as coupling paths for weakly coupled antennas. It furthermore provides a *predictive* visualization method of important regions for weak mutual coupling between antennas.

Predictive here means, in a perturbative sense, that a small absorber placed on a positive region will reduce the mutual coupling between the antennas. Furthermore, we also show that an absorber placed on a negative region will increase mutual coupling. This predictability is compared with the ability of the method based on the Poynting vector [12], [13]. The comparisons are shown through numerical simulations in CST Microwave Studio for different setups.

It is well known that the distribution of electromagnetic fields over a platform can be sensitive to small changes in the geometry. Such geometry changes can either increase or decrease the mutual coupling between antennas. Investigations of fields and/or currents from one antenna usually tend to have

Manuscript generated July 1, 2021. The work of J. Lundgren and J. Malmström has been supported by Saab Surveillance. The work of J.-M. Hannula has been supported by the Walter Ahlström Foundation. The work of B. L. G. Jonsson and J. Malmström has been funded in part by VINNOVA within the competence center ChaseOn under the project iAA.

J. Lundgren is with the Division of Electromagnetic Engineering, KTH Royal Institute of Technology, 100 44 Stockholm, Sweden, and also with Saab Surveillance, 107 24 Stockholm, Sweden (e-mail: jlu8@kth.se).

J. Malmström is with Saab Surveillance, 107 24 Stockholm, Sweden.

J.-M. Hannula and B. L. G. Jonsson are with the Division of Electromagnetic Engineering, KTH Royal Institute of Technology, 100 44 Stockholm, Sweden.

difficulties in predicting how geometry or material changes will impact the mutual coupling. This is natural since the electromagnetic behavior of *both* antennas is essential to obtain the mutual coupling, and the method presented here solves this issue.

This method to determine coupling paths generalizes the normalized impedance density in [10] and the coupling density coefficient (CC) in [11], both of which are based on the reciprocity theorem. A novel and attractive feature in this generalization is that its amplitude can be compared across frequencies since the quantity connects to the mutual coupling as expressed by the scattering parameter S_{21}. Another important extension in this work is that the proposed method handles arbitrary complex-valued self-impedances for the antennas, and also both well and poorly-matched impedances, which is directly linked to the mutual coupling as expressed by S_{21}. Both features are of particular interest when investigating out-of-band coupling, where the receiving antenna often is badly tuned [1]. The work in [11] mainly focuses on identifying coupling paths, whereas the work presented in this paper focuses on identifying, validating, and affecting the coupling and its paths. In order to mitigate coupling, we propose and illustrate here a new visualization-based method that involves the comparison of the vector-field associated with mutual coupling across frequencies. Another unique aspect of the present quantity is its ability to identify regions that contribute to an *increased* coupling in addition to regions that *reduce* the coupling. See Section III for illustrations and utilization of this feature. This paper emanates from the master thesis [22].

This paper is organized as follows. In Section II, the theory of the generalized impedance density and its connection to mutual coupling is explained. In Section III, the possibility to use the generalized impedance density to predict absorber placement that reduces the mutual coupling is investigated. This is done through numerical simulations for three different cases of increasing complexity. The predictability of the generalized impedance density is compared to the Poynting vector based method. Finally, our conclusions are presented in Section IV.

II. Theory

A. Mutual Coupling and Impedance Parameters

Mutual coupling, S_{21}, between two antenna ports is defined as the received power in one port, normalized with the transmitted power in the other port. The *isolation* between two antennas is defined as $1/|S_{21}|$. The corresponding impedance parameters connecting the two antenna ports are defined as

$$\begin{bmatrix} V_{11} \\ V_{21} \end{bmatrix} = \begin{bmatrix} Z_{11} & Z_{12} \\ Z_{21} & Z_{22} \end{bmatrix} \begin{bmatrix} I_{11} \\ I_{21} \end{bmatrix}. \tag{1}$$

Here, Z_{11} and Z_{22} are the self-impedances of Antenna 1 and Antenna 2, respectively, and Z_{12}, Z_{21} are the mutual impedances between the two antennas. The influence of each impedance parameter and the voltages V_{ij} and currents I_{ij} for $i, j = 1, 2$ is shown in Fig. 1 for a reciprocal two-port, where Z_0 is the reference impedance. From (1) and Fig. 1 it is seen that when no load is connected to Port 2, the mutual impedance is given by

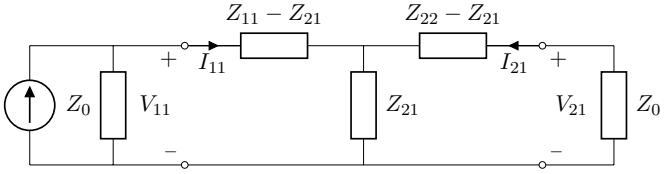

Fig. 1. A reciprocal two-antenna system seen as a two-port. The antennas and their mutual coupling are characterized by Z_{ij}, $i, j = 1, 2$. A non-ideal current source with impedance Z_0 is connected to Antenna 1 (Port 1) and a reference load Z_0 is connected to Antenna 2 (Port 2).

$$Z_{21} = \left.\frac{V_{21}}{I_{11}}\right|_{I_{21}=0} = \frac{V_{21}^{\mathrm{oc}}}{I_{11}^{\mathrm{oc}}} \tag{2}$$

and represents the coupled voltage in Port 2 due to a current in Port 1. The superscript "oc" refers to an open circuit condition.

Expanding the relation between scattering and impedance parameters [23] in a Taylor series, in the limit of small Z_{21}, Z_{12} gives the first-order approximation

$$S_{21} \approx Z_{21} \frac{2Z_0}{(Z_{11} + Z_0)(Z_{22} + Z_0)}, \tag{3}$$

which is valid when

$$|(Z_{11} + Z_0)(Z_{22} + Z_0)| \gg |Z_{21} Z_{12}|. \tag{4}$$

Here, Z_0 is the transmission line reference impedance, assumed to be real-valued and identical in the transmitter and receiver. For the case of antennas with typically reference impedance $Z_0 = 50\,\Omega$ and a small mutual coupling, this approximation is useful. For antennas on a platform, it is often desired that the mutual impedance Z_{21} is several orders of magnitude below the reference impedance Z_0. It is seen from (3) that the mutual impedance Z_{21} is to leading order proportional to S_{21} and it is therefore of interest to study Z_{21} when solving problems with weak antenna coupling.

B. Mutual Impedance and the Reaction Theorem

The mutual impedance is proportional to the reaction [21]. Since this relation is a key result in the derivation of the coupling-paths, the main steps are outlined below. The reciprocity theorem for electromagnetic fields [19] relates two sets of sources $\boldsymbol{J}_1$, $\boldsymbol{M}_1$ and $\boldsymbol{J}_2$, $\boldsymbol{M}_2$ that produce the fields $\boldsymbol{E}_1$, $\boldsymbol{H}_1$ and $\boldsymbol{E}_2$, $\boldsymbol{H}_2$ in a linear and isotropic surrounding medium by

$$\int_{v_1} (\boldsymbol{E}_2 \cdot \boldsymbol{J}_1 - \boldsymbol{H}_2 \cdot \boldsymbol{M}_1) \mathrm{d}v = \int_{v_2} (\boldsymbol{E}_1 \cdot \boldsymbol{J}_2 - \boldsymbol{H}_1 \cdot \boldsymbol{M}_2) \mathrm{d}v. \tag{5}$$

For the case of antennas, $\boldsymbol{J}_i$, $\boldsymbol{M}_i$ represents Antenna i that generates the fields $\boldsymbol{E}_i$, $\boldsymbol{H}_i$ for $i = 1, 2$. The volume v_1 includes Antenna 1 and v_2 includes Antenna 2. The right-hand side of (5) has been defined as the reaction

$$\langle 2, 1 \rangle = \int_{v_2} (\boldsymbol{E}_1 \cdot \boldsymbol{J}_2 - \boldsymbol{H}_1 \cdot \boldsymbol{M}_2) \mathrm{d}v \tag{6}$$

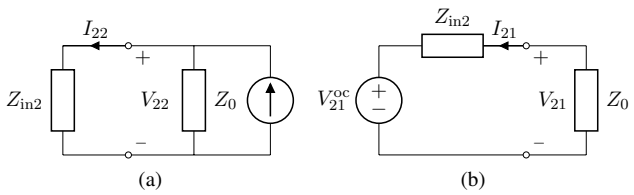

Fig. 2. (a) Non-ideal current source connected to Port 2 of the two-port circuit in Fig. 1. (b) Thevenin equivalent of the two-port circuit in Fig. 1.

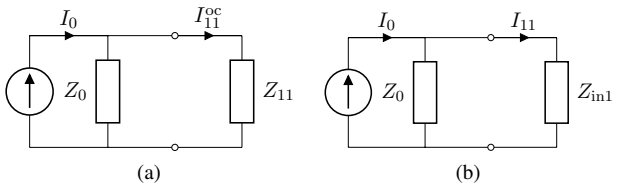

Fig. 3. Driving current in Port 1 when Port 2 is (a) an open circuit and (b) connected to a load.

of Port 1 on Port 2 [20], [21]. Utilizing Lorentz' reciprocity theorem [23], see Appendix, the reaction (6) can be expressed in terms of the fields as

$$\langle 2,1\rangle = \oint_{s_2} (\boldsymbol{E}_2 \times \boldsymbol{H}_1 - \boldsymbol{E}_1 \times \boldsymbol{H}_2) \cdot \hat{\boldsymbol{n}} \mathrm{d}s, \tag{7}$$

where s_2 is a surface that encloses Antenna 2 but not Antenna 1, and $\hat{\boldsymbol{n}}$ is an outward pointing normal to s_2.

The reaction of a two-port circuit is derived from (6) with sources $\boldsymbol{J}_2 \mathrm{d}v = I_{22}\mathrm{d}\boldsymbol{\ell}$, $\boldsymbol{M}_2 \mathrm{d}v = V_{22}\mathrm{d}\boldsymbol{\ell}$, analogously to [24, Ch. 3], as

$$\langle 2,1\rangle = V_{22}I_{21} - V_{21}I_{22}. \tag{8}$$

V_{22} and I_{22} correspond to a non-ideal current source connected to Port 2, i.e., interchanging the source and load in Fig. 1. Fig. 2(a) shows the non-ideal current source connected to Port 2, with the two-port network and the load Z_0 connected to Port 1 expressed as the input impedance

$$Z_{\rm in2} = Z_{22} - \frac{Z_{21}Z_{21}}{Z_{11}+Z_0} \tag{9}$$

in Port 2. The generalized reaction theorem [21] states that the reaction $\langle 2,1\rangle$ is independent of the load Z_0 connected to Port 2. This follows even though both V_{21} and I_{21} on the right-hand side of (8) are dependent on Z_0. The reason is that changes in V_{21} compensates any changes in I_{21} to cancel the effects of the value of Z_0. This property implies that letting $I_{21} = 0$ (open circuit at Antenna 2) will not affect the reaction. As an easy case to explicitly show this with the aid of the Thevenin theorem [23], consider the two-port circuit in Fig. 1. The two-port circuit and the current source connected to Port 1 are represented as a Thevenin equivalent as seen in Fig. 2(b), with the equivalent voltage $V_{21}^{\rm oc}$ and impedance $Z_{\rm in2}$, given by (9). From Fig. 2 it is clearly seen that

$$I_{22} = \frac{V_{22}}{Z_{\rm in2}}, \quad V_{21} = V_{21}^{\rm oc}\frac{Z_0}{Z_{\rm in2}+Z_0}, \quad I_{21} = -\frac{V_{21}}{Z_0}. \tag{10}$$

Inserting (9) and (10) into (8) and rearranging gives

$$\langle 2,1\rangle = -V_{21}^{\rm oc} I_{22} \tag{11}$$

as the generalized reaction theorem states [21]. The mutual impedance Z_{21} is calculated with the generalized reaction theorem by inserting (7) and (11) into (2) as

$$Z_{21} = \frac{-\langle 2,1\rangle}{I_{11}^{\rm oc} I_{22}} = \frac{-1}{I_{11}^{\rm oc} I_{22}} \oint_{s_2} (\boldsymbol{E}_2 \times \boldsymbol{H}_1 - \boldsymbol{E}_1 \times \boldsymbol{H}_2) \cdot \hat{\boldsymbol{n}} \mathrm{d}s, \tag{12}$$

which is the formulation used in [10], [21], [25], [26] for mutual impedance calculations. Note that the relation (12) contains an implicit constraint that the receiving antenna must be open circuit.

To overcome this constraint, a correction factor is derived for the case of non-ideal current sources or a load connected to the receiving antenna, i.e. $I_{21} \neq 0$. Fig. 3(a) shows the case when Port 2 is an open circuit and Fig. 3(b) shows the case when Port 2 is connected to a load. By expressing I_0 from Fig. 3(a,b) in terms of the loads and the driving current I_{11} and the open circuit driving current $I_{11}^{\rm oc}$, the following identity is obtained

$$I_{11}^{\rm oc}(Z_{11}+Z_0) = I_{11}(Z_{\rm in1}+Z_0). \tag{13}$$

The factor η is defined from the identity in (13) as

$$\eta = \frac{I_{11}}{I_{11}^{\rm oc}} = \left(\frac{Z_{11}+Z_0}{Z_{\rm in1}+Z_0}\right), \quad Z_{\rm in1} = Z_{11} - \frac{Z_{21}Z_{21}}{Z_{22}+Z_0}. \tag{14}$$

Inserting the factor η to (12) gives

$$Z_{21} = \frac{V_{21}}{I_{11}} = \frac{\eta}{I_{11}I_{22}} \oint_{s_2} (\boldsymbol{E}_1 \times \boldsymbol{H}_2 - \boldsymbol{E}_2 \times \boldsymbol{H}_1) \cdot \hat{\boldsymbol{n}} \mathrm{d}s. \tag{15}$$

Note that (15) does not contain any open-circuit constraints, but can be used with arbitrary port loads. This simplifies the simulation to determine the required fields in (15) and follows from the fact that the excitation of the antennas can be done sequentially with a non-ideal source and arbitrary loads for the same antenna geometry.

C. Coupling Visualization Using the Reaction Theorem

To determine Z_{21}, it suffices to calculate the integral in (15) over a surface s_2 that encloses Antenna 2 but not Antenna 1, which has been reported in [10], [21], [25]–[27]. A finite truncated plane can be used with a negligible loss of precision as an integration surface [10], which corresponds to one of the red planes in Fig. 4 that separates the two antennas into two disjoint regions. The normalized impedance density

$$\tilde{\varrho}_{21} = \frac{\boldsymbol{E}_1 \times \boldsymbol{H}_2 - \boldsymbol{E}_2 \times \boldsymbol{H}_1}{Z_{21} I_{11}^{\rm oc} I_{22}} \cdot \hat{\boldsymbol{n}} \tag{16}$$

was introduced and applied in [10] to identify coupling paths by visualizing $\tilde{\varrho}_{21}$ on separation planes between the antennas.

Here, a generalized form of the normalized impedance density is derived from (15) with the correction factor η that handles non-ideal current sources and an arbitrary load connected to the receiving antenna. Multiplying both sides of (15) with $Z_{21}^*/|Z_{21}|$ gives

$$|Z_{21}| = \oint_{s_2} \eta \frac{Z_{21}^*}{|Z_{21}|} \frac{\boldsymbol{E}_1 \times \boldsymbol{H}_2 - \boldsymbol{E}_2 \times \boldsymbol{H}_1}{I_{11}I_{22}} \cdot \hat{\boldsymbol{n}} \mathrm{d}s. \tag{17}$$

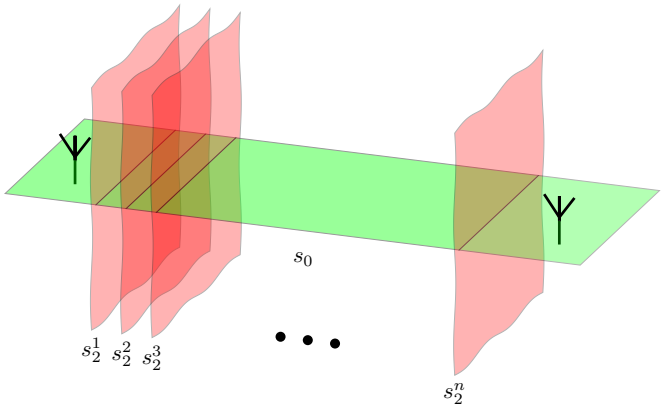

Fig. 4. Two antennas on a common platform with n red separation planes s_2 that construct a 3D representation of the coupling. The green plane s_0 illustrates a visualization plane.

The left-hand side of (17) is real-valued, which implies that the integral of the imaginary part must be zero and the only contribution to $|Z_{21}|$ comes from the real-part. Furthermore, the integral is strictly positive, i.e., the integrand is dominantly non-negative on the surface s_2. Omitting the imaginary part that will cancel out gives the following vector integrand

$$\boldsymbol{\delta}_{21} = \mathrm{Re}\left\{\eta \frac{Z_{21}^*}{|Z_{21}|} \frac{\boldsymbol{E}_1 \times \boldsymbol{H}_2 - \boldsymbol{E}_2 \times \boldsymbol{H}_1}{I_{11} I_{22}}\right\}. \tag{18}$$

Note that (18) does not contain the projection on the separation plane normal $\hat{\boldsymbol{n}}$. Hence, $\boldsymbol{\delta}_{21}$ is invariant of the separation surface s_2. The vector-field of $\boldsymbol{\delta}_{21}$ in $\mathbb{R}^3$ provides a direct visualization of the coupling that is straightforward to calculate, since η and (18) contain only fields, excitation currents and impedances. Projecting $\boldsymbol{\delta}_{21}$ on an arbitrary separation plane, as in Fig. 4, results in the scalar quantity

$$\delta_{21} = \boldsymbol{\delta}_{21} \cdot \hat{\boldsymbol{n}}, \tag{19}$$

which is a real-valued, and time-invariant quantity with dimension Ω/m^2 that varies with position.

Compared to the normalized impedance density $\tilde{\varrho}_{21}$ in (16), the quantity δ_{21} defined in (19) handles non-ideal current sources. With the introduced changes, δ_{21} will be referred to as a *generalized impedance density*. The normalization of δ_{21} makes it possible to compare the relative importance of coupling paths across frequencies, see Section III-C.

The relation between δ_{21} and Z_{21} can now be written as

$$|Z_{21}| = \oint_{s_2} \delta_{21} \, \mathrm{d}s. \tag{20}$$

According to (3), under the approximation (4), $S_{21} \propto Z_{21}$, and hence,

$$|S_{21}| \propto \oint_{s_2} \delta_{21} \, \mathrm{d}s. \tag{21}$$

From (21), it is clear that the generalized impedance density[1] δ_{21} describes the spatial distribution of $|S_{21}|$ over any separation surface s_2.

A 3D representation of the spatial variation of the mutual coupling contributions is constructed by calculating δ_{21} on several of the separation planes, from which it is possible to visualize the coupling on any plane, see e.g. the green plane s_0 in Fig. 4. It is important to remember that integrating (20) over a visualization plane s_0 will not yield Z_{21}. Nevertheless, it is useful for determining the distribution of how different regions in each vertical plane contribute to the mutual coupling and to provide a visualization of this information.

Note that δ_{21} depends on the normal $\hat{\boldsymbol{n}}$, associated with a separation surface s_2. Thus, in using δ_{21}, it is important to state which sequence of separating surfaces is used to determine the coupling paths. Any such sequence works since the integration over each s_2 gives $|Z_{21}|$. In the investigated cases in Section III, the separation planes (red) and visualization planes (green) similar to Fig. 4 are used.

[1]Note that the result can be extended to the strong coupling regime by replacing $Z_{21}^*/|Z_{21}|$ in (18) with

$$\frac{2Z_0}{(Z_{11}+Z_0)(Z_{22}+Z_0) - Z_{21}Z_{12}} \frac{S_{21}^*}{|S_{21}|} \tag{22}$$

resulting in that the proportionality in (21) becomes an equality. However, all considered examples in this work are in the weak coupling regime, and the results therefore use (18).

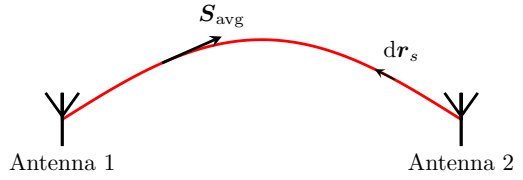

Fig. 5. The red line illustrates a streamline through the Poynting vector that visualizes the coupling path between Antenna 1 and Antenna 2.

D. The Poynting Vector Based Method

One method to generate coupling paths is to draw streamlines following the vector field described by the time-averaged Poynting vector [12], [13]. When Antenna 1 radiates, the power-flux goes from Antenna 1 to Antenna 2, and the streamline is thus the trace of the vector-field that connects back the power-flux that hits Antenna 2. A Poynting vector based coupling path can be determined from the relations

$$\mathrm{d}\boldsymbol{r}_s \times \boldsymbol{S}_{\mathrm{avg}} = 0, \quad \boldsymbol{S}_{\mathrm{avg}} = \frac{1}{2}\mathrm{Re}\{\boldsymbol{E}_1 \times \boldsymbol{H}_1^*\} \tag{23}$$

starting from the location of the receiving antenna port. Fig. 5 shows the notation and illustrates a streamline from Antenna 2 when Antenna 1 transmits.

III. Numerical Simulations

The goal of this section is to evaluate the ability of the generalized impedance density to predict coupling paths and absorber positions that decrease the mutual coupling. Results are compared to the Poynting vector based method.

A. Perforated Screen

The first configuration on which the generalized impedance density is tested consists of two dipole antennas separated

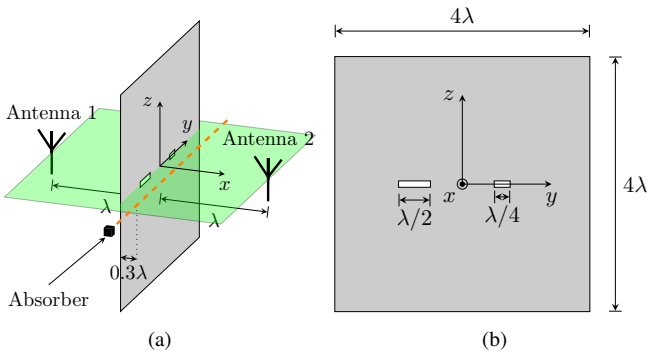

Fig. 6. A perforated screen that separates two dipole antennas. (a) The orange dashed line illustrates the path along which the black cube is swept. (b) Dimensions of the screen, where both slots have a height of $\lambda/10$.

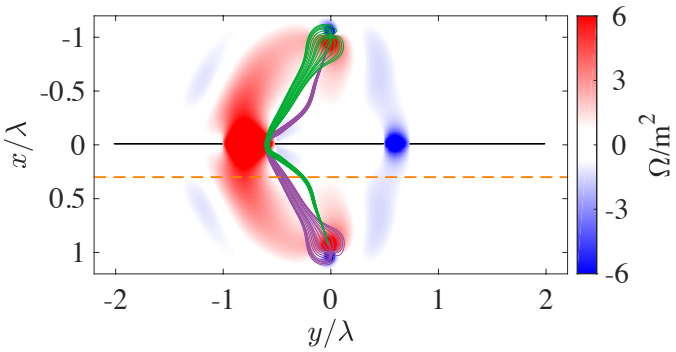

Fig. 7. Generalized impedance density δ_{21} on the green visualization plane in Fig. 6(a). The purple and green lines are 20 streamlines starting from the location of Antenna 1 and Antenna 2, respectively.

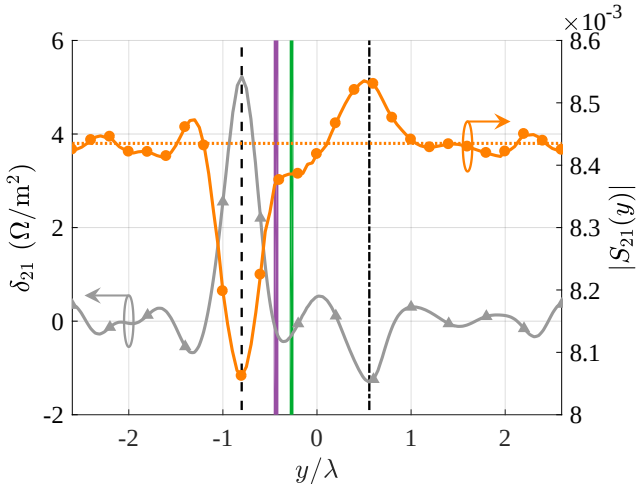

Fig. 8. Testing the predicted coupling contributions from the green plane in Fig. 6(a). The gray curve is δ_{21} at $x = 0.3\lambda$, $z = 0$. The orange curve with circles is the mutual coupling S_{21} as a function of the y position of the cube. The dashed horizontal line is $|S_{21}|$ for the unperturbed case. The purple and green vertical bars indicate where the streamlines in Fig. 7 pass.

by a perfect electrical conductor (PEC) screen as shown in Fig. 6(a). The screen has two slots of dimension $\lambda/4$ and $\lambda/2$, respectively, both with height $\lambda/10$, as shown in Fig. 6(b). The slots are separated by a distance λ.

The widths and orientations of the slots were chosen such that the larger slot has a larger contribution to the mutual coupling than the smaller one. The frequency considered is 300 MHz. The dipoles are identical with length 448 mm, radius 3 mm, resulting in the self-impedances $Z_{11} = Z_{22} = 65.7 - \mathrm{j}12.1\,\Omega$. The reference impedance is set to $Z_0 = 50\,\Omega$. The mutual impedance $Z_{21} = 0.67 - \mathrm{j}0.92\,\Omega$, which satisfies the weak-coupling relation in (3).

This case is used for an initial comparison of the two visualization methods described in Section II. A question here is in which way one can compare the correctness of the predicted coupling paths or regions that contribute to a larger coupling. The approach to answering this question is to use a small absorber as a tool to determine the impact of a spatial region's local contribution to the mutual coupling. The absorber used here is a cube with side 0.1λ and material parameters $\varepsilon_r = 1 - \mathrm{j}2$, $\mu_r = 1 - \mathrm{j}2$. This electrically small absorber provides a perturbation of the initial setup to directly indicate the regional sensitivity on the mutual coupling.

The coupling is visualized in the green xy-plane seen in Fig. 6(a). Fig. 7 depicts the generalized impedance density δ_{21} in the background calculated with (19). The surface normal of the yz-separation planes is $\hat{\boldsymbol{n}} = -\hat{\boldsymbol{x}}$. On the xy-visualization plane, δ_{21} has a positive (red) area that connects the two antennas through the larger slot and a negative (blue) region that connects the antennas through the smaller slot.

Poynting vector streamlines, based on (23), are also visualized in Fig. 7 as purple and green lines. The purple (green) lines connecting the two antennas through the larger slot are 20 streamlines when Antenna 1 (Antenna 2) transmits. The starting points of the streamlines are uniformly distributed on a circle located in the green xy-plane depicted in Fig. 6(a). The circle has a radius of $\lambda/100$ and is centered at the port location of the receiving antenna. Fig. 7 shows that the streamlines starting from Antenna 1 do not follow the same path as the streamlines starting from Antenna 2. This behavior is expected [18].

Now, all the tools required to evaluate the accuracy of the predicted regions with dominant contributions to the coupling are in place. The mutual coupling of the original problem is perturbed by moving the above-described absorber along the dashed line $x = 0.3\lambda, z = 0$ shown in Figs. 6 and 7. The orange curve with circles in Fig. 8 shows the mutual coupling $S_{21}(y)$ as a function of the position y of the absorber. The gray curve with triangle marks in Fig. 8 shows the generalized impedance density, δ_{21}, along the same dashed line. The vertical purple and green lines indicate where the streamlines in Fig. 7 pass $x = 0.3\lambda$.

The first thing to notice in Fig. 8 is the agreement between the generalized impedance density and the mutual coupling. The black dashed vertical line highlights the correlation between the positive peak of the generalized impedance density (indicating strong coupling) and the maximal reduction region of the mutual coupling. An absorber placed in this region will have the best effect on reducing the mutual coupling.

Furthermore, Fig. 8 shows that when the cube is located in the most negative generalized impedance density, the mutual

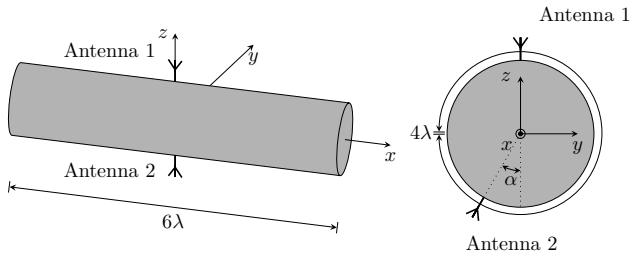

Fig. 9. A PEC cylinder with two monopoles located in the yz-plane and equally far from the edges of the cylinder. Antenna 2 is rotated $\alpha = 11.25°$ from the bottom.

coupling is increased, as highlighted with the black vertical dash-dotted line.

Finally, placing the cube on the Poynting vector streamlines, i.e., the purple and green vertical lines in Fig. 8, only has a minor impact on the mutual coupling in this configuration.

It has thus been demonstrated that it is possible to predict regions with strong coupling. The method used shows that it is possible to predict absorber locations that will either decrease or increase the mutual coupling by inspecting δ_{21}. Visualizing δ_{21} on a plane that consists of several separation planes, as proposed in Section II, provides insight into how the coupling is distributed between the antennas. By using δ_{21}, as seen from Fig. 8, the contribution through the smaller slot partially cancels the coupling through the larger slot at the investigated frequency.

B. Cylinder model

To investigate how the presence of a platform impacts the coupling visualization, a PEC cylinder is used as a platform with two monopole antennas mounted on it, one antenna on the top and one at the bottom, as shown in Fig. 9. The cylinder is 6λ long and has a 4λ circumference at 18 GHz. Perfectly matched layer (PML) boundary conditions are applied to the ends of the cylinder in the x-direction to reduce edge effects. The two monopoles are identical with length 3.6 mm, and radius 0.05 mm. Both antennas are located equally far from the edges of the cylinder. Antenna 2 is rotated an angle $\alpha = 11.25°$ along the cylinder axis from the bottom to introduce a length difference between the power flowing on the left- and right-hand side of the cylinder. The self-impedances $Z_{11} = Z_{22} = 37.2 + \mathrm{j}1.5\,\Omega$ and the reference impedance $Z_0 = 50\,\Omega$ with a mutual impedance $Z_{21} = 0.35 - \mathrm{j}0.37\,\Omega$, which satisfy the weak-coupling requirement in (3).

The coupling is visualized both with the generalized impedance density and the Poynting vector based method. The case illustrated here is for the yz-visualization plane that contains both the antennas, where Fig. 10(a) depicts the generalized impedance density δ_{21} computed with (19), using the xy-separation planes with $\hat{\boldsymbol{n}} = \hat{\boldsymbol{z}}$. Fig. 10(b) depicts the magnitude of $\boldsymbol{S}_{\mathrm{avg}}$ computed with (23) when Antenna 2 at the bottom transmits. The green lines in Fig. 10(b) are 40 streamlines computed with (23) that start from the port location of Antenna 1. The starting points are uniformly

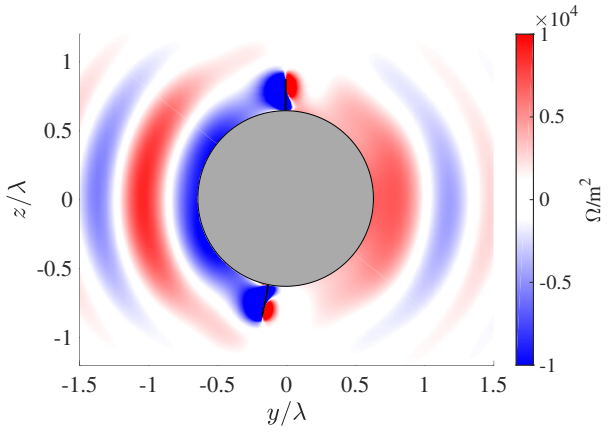

(a)

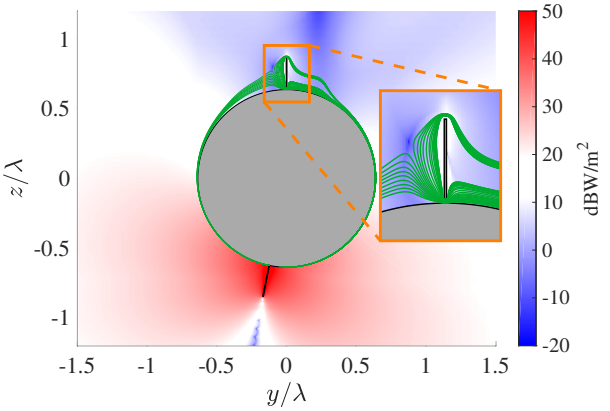

(b)

Fig. 10. Visualization in the yz-plane that contains both the antennas, at 18 GHz. (a) Generalized impedance density δ_{21}. (b) Magnitude of $\boldsymbol{S}_{\mathrm{avg}}$ in the background with green streamlines when Antenna 2 transmits.

distributed over two lines parallel to the port of Antenna 1, i.e. along the z-axis. The lines are located at a distance $\lambda/20$ from the port on the left- and right-hand side respectively.

Fig. 10(a) shows that the right- (left-) hand side of the cylinder has a positive (negative) contribution. From the conclusions in Section III-A and the relation (3), it is therefore expected that placing an absorber on the left (right) hand side would increase (decrease) the mutual coupling. The streamlines of the Poynting vector are flowing on both sides of the cylinder as seen in Fig. 10(b). The inset figure shows that 9 of the 40 streamlines are flowing on the left-hand side. Thus, the streamlines indicate a high coupling between the antennas on both sides of the cylinder, whereas the generalized impedance density indicates that only the right-hand side contributes to an increased coupling. To validate these two different predictions, we add an absorber to the left- or right-hand side, respectively, to one side of the cylinder at the time. Fig. 11(a) depicts the absorbers on the left- and right-hand side located equally far from the cylinder edges with length $L = \lambda$, width $w = 0.5\lambda$, and thickness $t = 1$ mm. The absorber used in this case is a Laird Q-Zorb 2338 surface wave absorbing material (SWAM) [28] that is intended for attenuating surface waves with material

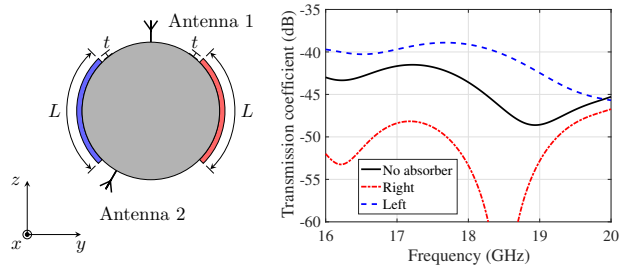

Fig. 11. (a) Absorbers with $L = \lambda$, $t = 1\,\text{mm}$, and width $w = 0.5\lambda$ along x. (b) S_{21} when the absorbers from (a) is added on one side at the time on the cylinder.

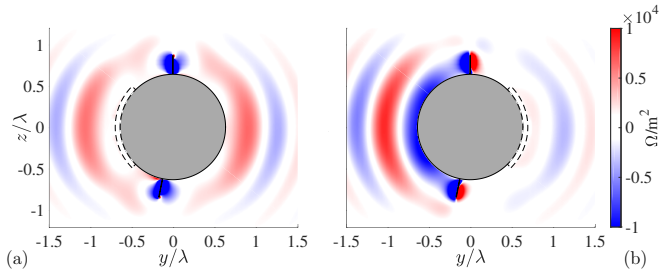

Fig. 12. Visualization of δ_{21} in the yz-plane that contains both the antennas, at 18 GHz when the absorber is added on the (a) left-hand side. (b) right-hand side.

parameters $\varepsilon_r = 14.4 - \text{j}0.26$, $\mu_r = 1.44 - \text{j}1.01$ at 18 GHz. The complete frequency behavior of this absorber can be found in [22] and the material library of CST Microwave Studio. The weak-coupling relation in (3) is satisfied.

Fig. 11(b) shows that placing the absorber on the right-hand side decreases the coupling, and that placing the absorber on the left-hand side increases the coupling at 18 GHz, as predicted by the generalized impedance density, δ_{21} in Fig. 10(a). The effects on the antenna self-impedances Z_{11}, Z_{22} are below $0.8\,\Omega$ (2.2 %) in magnitude and 1.2° in phase when introducing the absorbers. The main contribution to the change in $|S_{21}|$ hence comes from the reduction in Z_{21}. Thus, similar to the previous case in Section III-A, we see that the generalized impedance density can be used to locate regions which contribute to high coupling. In the present case, we note that the streamlines, using (23) could only partly predict regions of strong coupling.

In Fig. 12(a), δ_{21} is visualized with an absorber placed on the left-hand side, as highlighted with the black dashed line. The region close to the surface on the left-hand side of the cylinder has turned from a negative generalized impedance density region, depicted as blue in Fig. 10(a), to a positive region, as depicted with red and white. The contribution from this area is now positive, leading to an increased mutual coupling. Fig. 12(b) illustrates δ_{21} when the absorber is placed on the right-hand side. The large red area close to the surface on the right-hand side in Fig. 10(a) is reduced, resulting in a decreased coupling.

It has been demonstrated that the generalized impedance density δ_{21} is a useful tool when predicting absorber positions

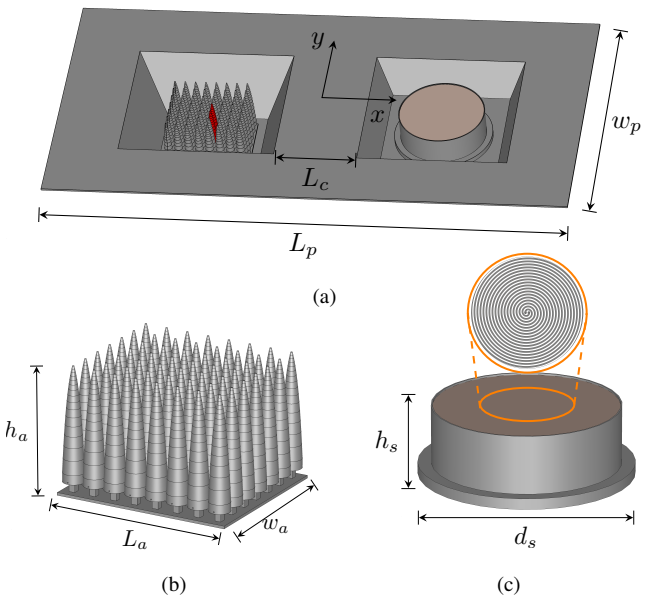

Fig. 13. (a) Section of a platform with two integrated antennas. Platform dimensions is $L_p = 310\,\text{mm}$, $w_p = 160\,\text{mm}$, and the distance between the cavities is $L_c = 49\,\text{mm}$. (b) BOR-array antenna with 6x8 elements and $L_a = 50\,\text{mm}$, $w_a = 43\,\text{mm}$, and $h_a = 35\,\text{mm}$. (c) Cavity-backed spiral antenna with diameter $d_s = 52\,\text{mm}$ and $h_s = 19.2\,\text{mm}$.

that reduce the mutual coupling as well as increase the coupling. Visualizing δ_{21} is also a useful for larger perturbations of the platform, in this case with larger absorbers. We conclude that the visualization method can be used to obtain accurate information for reducing the mutual coupling, contrary to what is claimed in [11].

C. Integrated Antennas

The third case is a more complex configuration consisting of a ground plane with two cavities for integrating antennas, as seen in Fig. 13. The configuration could represent a section of an integrated mast of a naval ship, as well as a wingtip on an aircraft or a part of its fuselage.

The possibility of using the generalized impedance density to predict where to place absorbers to reduce the mutual coupling between two wideband antennas integrated in the platform is investigated here. A 6×8 element body-of-revolution (BOR) array antenna [29], [30], depicted in Fig. 13(b), is used and referred to as Antenna 1. The other antenna is a cavity-backed spiral antenna that is shown in Fig. 13(c) and is referred to as Antenna 2. The center of the spiral, depicted in the orange inset in Fig. 13(c), is designed to intrinsically generate left-hand circular polarization. Both antennas are placed in their respective cavities seen in Fig. 13(a) with the top of the antennas located 1.2 mm below the surface of the platform.

The mutual coupling between a center element in the array, which is highlighted red in Fig. 13(a), and the spiral antenna is studied. The other array elements are terminated with a matched load. Potential absorber locations have been restricted to the flat section between the two cavities. The considered frequency range is 10–14 GHz. For the described configuration, the condition (3) is satisfied.

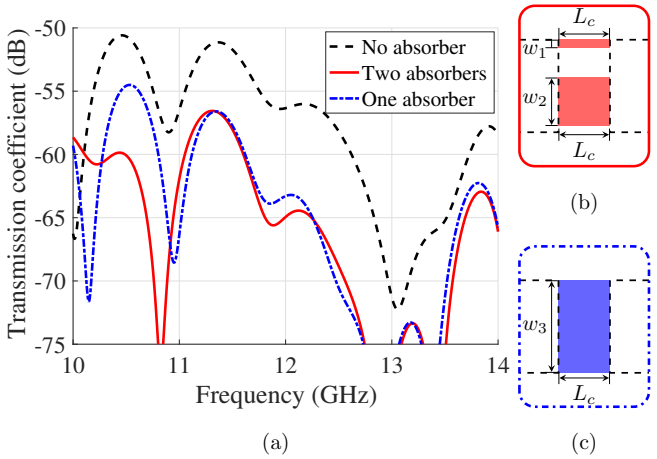

Fig. 14. (a) Transmission coefficient between the array element and the spiral without absorbers (black dashed), with two absorbers according to Fig. 14(b) (red solid), and with one absorber according to Fig. 14(c) (blue dash-dotted). (b) Absorbers placed based on δ_{21}. (c) An absorber covering the surface between the cavities.

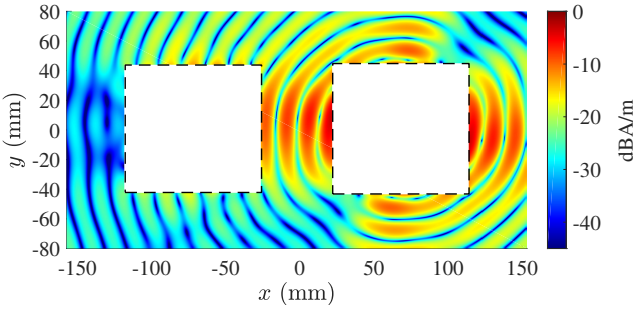

Fig. 15. Magnitude of the instantaneous surface currents on the platform generated by the spiral antenna at 10.5 GHz.

Predicting good absorber positions to reduce the mutual coupling between two antennas is a common and challenging task. The initial mutual coupling between the antennas is shown in Fig. 14(a) as the black dashed curve, with the highest coupling at 10.5 GHz and two other peaks at 11.25 GHz, and 14 GHz. One can approach this problem by investigating the surface currents. However, studying the surface currents of the spiral antenna on the flat surface of the platform at 10.5 GHz shows that the entire region contains strong surface currents, see Fig. 15. Similar behavior is observed in other frequencies in the band. From this type of information, it is difficult to determine if there is a preferred region to place absorbers on to reduce the mutual coupling.

In contrast, if the generalized impedance density δ_{21} is visualized, clear regions for absorber placement emerge. Fig. 16 shows δ_{21} for $z = 1$ mm above the platform, at the frequencies of the aforementioned peaks in the coupling. The black dashed lines highlight the location of the cavities and the antennas. The surface normal is $\hat{\boldsymbol{n}} = -\hat{\boldsymbol{x}}$, corresponding to a sequence of yz-separation planes that are used to construct the xy-visualization plane seen in Fig. 16. This choice of separation-planes is natural since the platform is modeled as a good

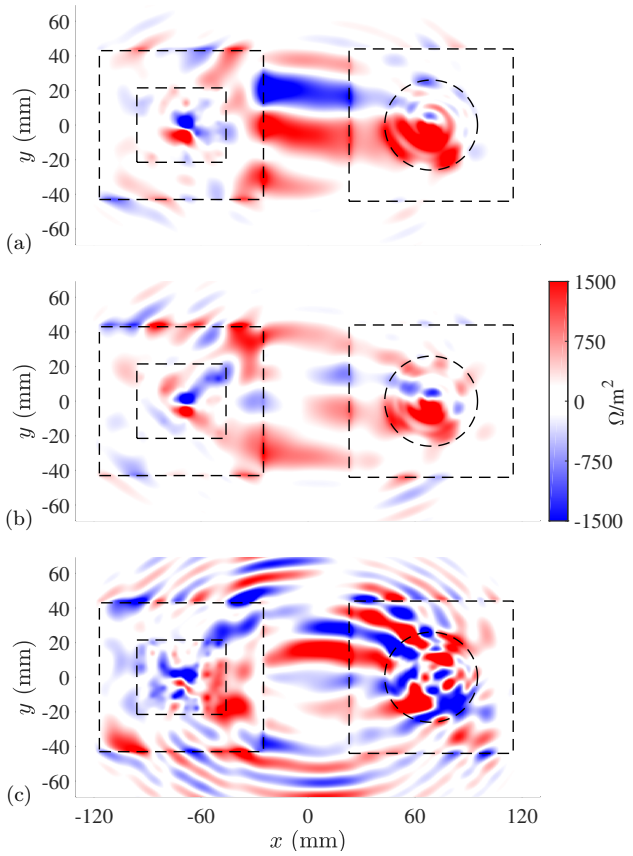

Fig. 16. Visualization of δ_{21} in the xy-plane for $z = 1$ mm above the platform at (a) 10.5 GHz, (b) 11.25 GHz, and (c) 14.0 GHz.

conductor.

Note that for 10.5 GHz, the dominant positive (red) region is at $y = 40$ mm and below $y = 8$ mm. The same regions in 11.25 GHz are also dominantly positive. A close look at 14.0 GHz shows that a smaller lower region 8 to -38 mm has mainly positive generalized impedance density with some weakly negative δ_{21}. For $y = 40$ mm, there is both a weak negative and a strong positive region.

Based on the visualization results in Fig. 16, absorbers are placed according to Fig. 14(b). The upper absorber has a width $w_1 = 8$ mm and is centered at $x = 0$ mm, $y = 40$ mm. The lower absorber has a width $w_2 = 46$ mm, and is centered at $x = 0$ mm, $y = -15$ mm. Both absorbers have a thickness of 1 mm and length $L_c = 49$ mm. The type of absorber used is the same SWAM [28], which is used in Section III-B. The red solid curve in Fig. 14(a) represents a simulation of the transmission coefficient with the absorbers placed according to Fig. 14(b). The mutual coupling is reduced in the frequency range 10.2–14 GHz when the absorbers are placed based on the visualization of the generalized impedance density in Fig. 16.

By comparing the intensity (color) of the generalized impedance density in the regions $y = 40$ mm and $y = [-38, 8]$ mm in Fig. 16(ab), it is clear that δ_{21} is much more positive in these regions at 10.5 GHz than at 11.25 GHz. From this fact, it is straightforward to understand the 9 dB versus 5 dB reduction differences between 10.5 GHz and 11.25 GHz

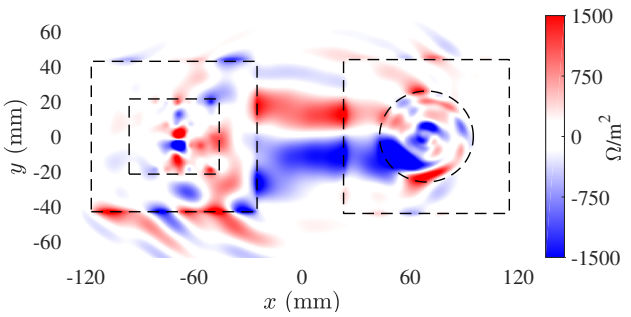

Fig. 17. Visualization of δ_{21} in the xy-plane for $z = 1$ mm above the platform at 10.0 GHz.

in Fig. 14(a).

The more standard approach of covering the whole surface between the two cavities with an absorber is also investigated. An absorber with length $L_c = 49$ mm, width $w_3 = 88$ mm, and thickness 1 mm is placed between the cavities as shown in Fig. 14(c). The blue dash-dotted curve in Fig. 14(a) is the simulated mutual coupling with the absorber in Fig. 14(c) present. The mutual coupling is 5 dB higher at 10.5 GHz when the whole surface is covered by an absorber, compared to placing absorbers according to Fig. 14(b), which is based on the generalized impedance density. Covering the whole surface between the cavities with an absorber reduces the negative generalized impedance density region centered at $y = 20$ mm in Fig. 16(a). This explains why the mutual coupling is higher compared to placing absorbers according to Fig. 14(b), as predicted by the generalized impedance density. At 11.25 GHz and 14 GHz, it is seen in Figs. 16(b) and (c) that an absorber covering the whole surface will reduce both red and blue regions, which describes why the difference between the two absorber configurations are small in terms of mutual coupling at 11.25 GHz and 14 GHz.

The absorber placement described above successfully reduces the coupling at the investigated frequencies. However, it results in an increased mutual coupling at 10 GHz, as shown in Fig. 14(a). This can be explained by inspecting the generalized impedance density at 10 GHz, see Fig. 17. The regions where the absorbers are placed are mainly negative (blue) at this frequency, leading to an increased mutual coupling.

Thus, the generalized impedance density has been used to systematically reduce the mutual coupling between two wideband antennas placed on a common platform with a satisfying result. By visualizing the generalized impedance density δ_{21} at several frequencies, it is possible to predict absorber positions that reduce the mutual coupling over a band of frequencies.

IV. Conclusion

In this paper, we generalize and evaluate a visualization method for identifying regions around a platform with large contributions to the mutual coupling between installed antennas. The presented real-valued time-invariant quantity δ_{21} (19) is named the generalized impedance density. The direct connection between the reciprocity theorem and the mutual coupling is revisited, including a derivation of the generalized impedance density.

The generalized impedance density captures the interaction between fields and represents all the mechanisms that contribute to the coupling between antennas. It can be used to visualize how the mutual coupling is spatially distributed between the antennas.

The generalized impedance density has here been tested in numerical simulations to calculate coupling paths and predict absorber positions in three different cases. With the generalized impedance density, it is possible to separate the positive and negative coupling paths. This novel feature has been used to systematically reduce the mutual coupling between two antennas. The visualization method presented in this paper predicts good absorber locations, as expected from the derivation. Indeed, placing a small absorber at the strongest predicted generalized impedance density position gave a larger reduction of the mutual coupling than when the same absorber was placed at the position predicted by the Poynting vector based method. It is also clearly demonstrated that it is possible to achieve a lower mutual coupling with less absorber material when placing absorbers based on predictions by the generalized impedance density, compared to covering all available space with absorbers.

From the here presented examples, it is clear that the generalized impedance density provides important coupling information, which is robust to the platform shape. The proposed quantity offers the possibility to compare coupling paths at different frequencies. This useful feature makes it possible to reduce the coupling over a band of frequencies. It is furthermore easy to implement as a post-processing step in full-wave electromagnetic software.

The ability to distinguish between regions where the placement of absorbers would reduce or increase the mutual coupling, together with the straightforward interpretation of the results, makes the generalized impedance density a useful tool to visualize and systematically reduce the mutual coupling.

Appendix

For a set of sources $\boldsymbol{J}_2$, $\boldsymbol{M}_2$ in the volume v_2, the associated fields $\boldsymbol{E}_2, \boldsymbol{H}_2$ satisfy Maxwell's equations

$$\nabla \times \boldsymbol{E}_2 = -\mathrm{j}\omega\mu\boldsymbol{H}_2 - \boldsymbol{M}_2, \ \nabla \times \boldsymbol{H}_2 = \mathrm{j}\omega\varepsilon\boldsymbol{E}_2 + \boldsymbol{J}_2. \quad (24)$$

The fields $\boldsymbol{E}_1$, $\boldsymbol{H}_1$ are source-free in v_2, thus

$$\nabla \times \boldsymbol{E}_1 = -\mathrm{j}\omega\mu\boldsymbol{H}_1, \ \nabla \times \boldsymbol{H}_1 = \mathrm{j}\omega\varepsilon\boldsymbol{E}_1. \quad (25)$$

Recall the divergence of a cross-product:

$$\nabla \cdot (\boldsymbol{E} \times \boldsymbol{H}) = \boldsymbol{H} \cdot \nabla \times \boldsymbol{E} - \boldsymbol{E} \cdot \nabla \times \boldsymbol{H}. \quad (26)$$

Using (24), (25), and the divergence identity (26) gives

$$\nabla \cdot (\boldsymbol{E}_2 \times \boldsymbol{H}_1 - \boldsymbol{E}_1 \times \boldsymbol{H}_2) = \boldsymbol{E}_1 \cdot \boldsymbol{J}_2 - \boldsymbol{H}_1 \cdot \boldsymbol{M}_2, \quad (27)$$

from where (7) follows by the divergence theorem.

REFERENCES

[1] T. M. Macnamara, *Introduction to antenna placement and installation*, Chichester, UK: John Wiley & Sons, 2010.

[2] E. F. W. Alexanderson, "Simultaneous sending and receiving," *Proc. IRE*, vol. 7, no. 4, pp. 363–378, 1919.

[3] Z. Li, Z. Du, M. Takahashi, K. Saito, and K. Ito, "Reducing mutual coupling of MIMO antennas with parasitic elements for mobile terminals," *IEEE Trans. Antennas Propag.*, vol. 60, no. 2, pp. 473–481, 2012.

[4] S. Zhang, Z. Ying, J. Xiong, and S. He, "Ultrawideband MIMO/diversity antennas with a tree-like structure to enhance wideband isolation," *IEEE Antennas Wireless Propag. Lett.*, vol. 8, pp. 1279–1282, 2009.

[5] E. Rajo-Iglesias, O. Quevedo-Teruel, and L. Inclan-Sanchez, "Mutual coupling reduction in patch antenna arrays by using a planar EBG structure and a multilayer dielectric substrate," *IEEE Trans. Antennas Propag.*, vol. 56, no. 6, pp. 1648–1655, 2008.

[6] J. Zhang, S. Yan, X. Hu, and G. A. Vandenbosch, "Mutual coupling suppression for on-body multiantenna systems," *IEEE Trans. Electromagn. Compat.*, vol. 62, no. 4, pp. 1045–1054, 2020.

[7] H. H. Park, "Reduction of electromagnetic noise coupling to antennas in metal-framed smartphones using ferrite sheets and multi-via EBG structures," *IEEE Trans. Electromagn. Compat.*, vol. 60, no. 2, pp. 394–401, 2018.

[8] D. Sievenpiper, L. Zhang, R. F. Broas, N. G. Alexopolous, and E. Yablonovitch, "High-impedance electromagnetic surfaces with a forbidden frequency band," *IEEE Trans. Microw. Theory Techn.*, vol. 47, no. 11, pp. 2059–2074, 1999.

[9] H. Frid, "Analysis and optimization of installed antenna performance," Ph.D. dissertation, KTH Royal Institute of Technology, 2020.

[10] J. Malmström, H. Holter, and B. L. G. Jonsson, "On mutual coupling and coupling paths between antennas using the reaction theorem," *IEEE Trans. Electromagn. Compat.*, vol. 60, no. 6, pp. 2037–2040, 2018.

[11] Y. Zhong, W. Song, C. Kim, and C. Hwang, "Coupling path visualization and its application in preventing electromagnetic interference," *IEEE Trans. Electromagn. Compat.*, vol. 62, no. 4, pp. 1485–1492, 2020.

[12] H. Li, V. V. Khilkevich, and D. Pommerenke, "Identification and visualization of coupling paths—part I: Energy parcel and its trajectory," *IEEE Trans. Electromagn. Compat.*, vol. 56, no. 3, pp. 622–629, 2014.

[13] H. Li, V. V. Khilkevich, and D. Pommerenke, "Identification and visualization of coupling paths—part II: Practical application," *IEEE Trans. Electromagn. Compat.*, vol. 56, no. 3, pp. 630–637, 2014.

[14] T. Kurner, D. J. Cichon, and W. Wiesbeck, "Concepts and results for 3D digital terrain-based wave propagation models: An overview," *IEEE J. Sel. Areas Commun.*, vol. 11, no. 7, pp. 1002–1012, 1993.

[15] V. Degli-Esposti, D. Guiducci, A. de'Marsi, P. Azzi, and F. Fuschini, "An advanced field prediction model including diffuse scattering," *IEEE Trans. Antennas Propag.*, vol. 52, no. 7, pp. 1717–1728, 2004.

[16] A. Talebzadeh, P. C. Sochoux, J. Li, Q. Liu, K. Ghosh, and D. Pommerenke, "Shielding effectiveness, coupling path, and EMI mitigation for QSFP cages with heatsink," *IEEE Trans. Electromagn. Compat.*, vol. 60, no. 5, pp. 1254–1262, 2018.

[17] A. Talebzadeh, P. K. Vuppunutala, K. Koo, H. Li, J. Nadolny, Q. Liu, J. Li, K. Ghosh, P. C. Sochoux, V. Khilkevich *et al.*, "Coupling path visualization and EMI mitigation for flyover QSFP connectors," *IEEE Trans. Electromagn. Compat.*, vol. 62, no. 4, pp. 1037–1044, 2020.

[18] H. Li, V. Khilkevich, D. Pommerenke, Y. Zhang, and J. Fan, "On the possibility to detect and visualize electromagnetic coupling paths," in *Proc. IEEE Int. Symp. Electromagn. Compat.*, Aug. 2011, pp. 559–563.

[19] J. R. Carson, "Reciprocal theorems in radio communication," *Proc. IRE*, vol. 17, no. 6, pp. 952–956, 1929.

[20] V. H. Rumsey, "Reaction concept in electromagnetic theory," *Phys. Rev.*, vol. 94, no. 6, pp. 1483–1491, 1954.

[21] J. H. Richmond, "A reaction theorem and its application to antenna impedance calculations," *IRE Trans. Antennas Propag.*, vol. 9, no. 6, pp. 515–520, 1961.

[22] J. Lundgren, "Visualizing and controlling coupling paths between antennas installed on common platforms," M.S. thesis, Division Electromagn. Eng., KTH Royal Institute of Technology, Stockholm, Sweden, Jun. 2020.

[23] R. E. Collin, *Foundations for microwave engineering*, New York, NY, USA: John Wiley & Sons, 2007.

[24] R. F. Harrington, *Time-harmonic electromagnetic fields*, New York, NY, USA: McGraw-Hill, 1961.

[25] L. D. Bamford, P. S. Hall, and A. Fray, "Calculation of antenna mutual coupling from radiated far fields," in *Proc. 2nd Int. Conf. Comput. Electromagn.*, 1994, pp. 263–266.

[26] H. Yuan, H. Zhou, H. Liu, X. Dang, and X. Chen, "Computing mutual impedance of antennas by spherical harmonic transform," *IEEE Trans. Antennas Propag.*, vol. 67, no. 7, pp. 4377–4384, 2019.

[27] J. Malmström, "Derivation of reaction theorems for scattered fields," *IEEE Antennas Wireless Propag. Lett.*, vol. 17, no. 10, pp. 1876–1880, 2018.

[28] *"Microwave Absorbing Materials"* Laird Technologies. Accessed on: Nov. 4, 2020. [Online]. Available: https://www.mouser.com/pdfdocs/LairdEMIAbsorbers-2.pdf.

[29] H. Holter, "Dual-polarized broadband array antenna with BOR-elements, mechanical design and measurements," *IEEE Trans. Antennas Propag.*, vol. 55, no. 2, pp. 305–312, 2007.

[30] H. Frid, J. Malmström, and B. L. G. Jonsson, "Determining direction-of-arrival accuracy for installed antennas by postprocessing of far-field data," *Radio Sci.*, vol. 54, no. 12, pp. 1204–1221, 2019.